Solar Phys (2012) 279:295–316
DOI 10.1007/s11207-012-9976-x

Comparison of Line-of-Sight Magnetograms Taken by the *Solar Dynamics Observatory/Helioseismic and Magnetic Imager* and *Solar and Heliospheric Observatory/Michelson Doppler Imager*

Y. Liu · J.T. Hoeksema · P.H. Scherrer · J. Schou · S. Couvidat · R.I. Bush · T.L. Duvall Jr · K. Hayashi · X. Sun · X. Zhao

Received: 21 September 2011 / Accepted: 19 March 2012 / Published online: 6 April 2012

Abstract We compare line-of-sight magnetograms from the *Helioseismic and Magnetic Imager* (HMI) onboard the *Solar Dynamics Observatory* (SDO) and the *Michelson Doppler Imager* (MDI) onboard the *Solar and Heliospheric Observatory* (SOHO). The line-of-sight magnetic signal inferred from the calibrated MDI data is greater than that derived from the HMI data by a factor of 1.40. This factor varies somewhat with center-to-limb distance. An upper bound to the random noise for the $1''$ resolution HMI 720-second magnetograms is 6.3 Mx cm^{-2}, and 10.2 Mx cm^{-2} for the 45-second magnetograms. Virtually no *p*-mode leakage is seen in the HMI magnetograms, but it is significant in the MDI magnetograms. 12-hour and 24-hour periodicities are detected in strong fields in the HMI magnetograms. The newly calibrated MDI full-disk magnetograms have been corrected for the zero-point offset and underestimation of the flux density. The noise is 26.4 Mx cm^{-2} for the MDI one-minute full-disk magnetograms and 16.2 Mx cm^{-2} for the five-minute full-disk magnetograms observed with four-arcsecond resolution. The variation of the noise over the Sun's disk found in MDI magnetograms is likely due to the different optical distortions in the left- and right-circular analyzers, which allows the granulation and *p*-mode to leak in as noise. Saturation sometimes seen in sunspot umbrae in MDI magnetograms is caused by the low intensity and the limitation of the onboard computation. The noise in the HMI and MDI line-of-sight magnetic-field synoptic charts appears to be fairly uniform over the entire map. The noise is 2.3 Mx cm^{-2} for HMI charts and 5.0 Mx cm^{-2} for MDI charts. No evident periodicity is found in the HMI synoptic charts.

Keywords Solar magnetic fields photosphere · HMI magnetograms · MDI magnetograms

Y. Liu (✉) · J.T. Hoeksema · P.H. Scherrer · J. Schou · S. Couvidat · R.I. Bush · K. Hayashi · X. Sun · X. Zhao
HEPL, Stanford University, Stanford, CA 94305-4085, USA
e-mail: yliu@sun.stanford.edu

T.L. Duvall Jr
Solar Physics Laboratory, NASA Goddard Space Flight Center, Greenbelt, MD 20771, USA

1. Introduction

The observation program of the *Michelson Doppler Imager* (MDI) onboard the *Solar and Heliospheric Observatory* (SOHO) (Scherrer *et al.*, 1995) was terminated on 12 April 2011, after having continuously measured the Doppler velocity, longitudinal magnetic field, and intensity of the Sun for 15 years (except for several months interruption during the SOHO "vacation" in 1998). The data have been widely used for research and space-weather forecasting. The enhanced *Helioseismic and Magnetic Imager* (HMI: Scherrer *et al.*, 2012; Schou *et al.*, 2012) onboard the *Solar Dynamics Observatory* (SDO: Pesnell, Thompson, and Chamberlin, 2012) began making its routine observations on 30 April 2010. HMI data include all MDI observables, but with much higher spatial and temporal resolutions and better data quality. A comparison of the observational data between the two instruments is necessary in order to extend the research and space-weather modeling from the MDI data to the HMI data. In this article we compare the HMI and MDI line-of-sight magnetograms.

This article is organized as follows: Section 2 gives a detailed description of the HMI line-of-sight magnetograms, including the algorithm used to derive the magnetograms, the noise level, and issues that we have found. Since corrections were made to the MDI magnetograms in past years, such as corrections for the zero-point offset and for the spatially dependent underestimation of the flux density, we describe in Section 3 those changes in more detail. A comparison between MDI and HMI magnetograms is presented in Section 4. We summarize this work in Section 5.

2. HMI Line-of-Sight Magnetograms

The HMI instrument (Schou *et al.*, 2012) is a filtergraph with full-disk coverage by 4096×4096 pixels. The spatial resolution is $1''$ with a $0.5''$ pixel size. The spectral line is the Fe I 6173 Å absorption line formed in the photosphere (Norton *et al.*, 2006), and the width of the filter profiles is 76 mÅ. There are two CCD cameras in the instrument: the "front camera" and the "side camera". The front camera acquires filtergrams at six wavelengths spanning the spectral line in two polarization states, left-circular polarization (LCP) and right-circular polarization (RCP), with 3.75 seconds between the images. It takes 45 seconds to acquire a complete set of 12 filtergrams, which are transmitted to the ground. Dopplergrams and line-of-sight magnetograms are derived from this set of registered filtergrams, as are values for line width, line depth, and continuum intensity. The side camera is dedicated to measuring the vector magnetic field. The current frame list takes 135 seconds to obtain the filtergrams in six polarization states at six wavelength positions. The Stokes parameters $[I, Q, U, V]$ are computed from those measurements, and are further inverted (Borrero *et al.*, 2011) and disambiguated (Metcalf *et al.*, 2006; Leka *et al.*, 2009) to retrieve the vector magnetic field. To suppress p modes and increase the signal-to-noise ratio, usually the registered filtergrams are averaged over a certain time before computing the Stokes vector. Currently an average is computed every 720 seconds using a temporal filter applied to 1215 seconds of data (Couvidat *et al.*, 2012a). The side camera filtergrams are also used to compute Dopplergrams, intensities, and line-of-sight magnetograms using the same algorithm as the front camera. In this article, we use 45-second magnetograms to refer to the line-of-sight magnetograms from the front camera and 720-second magnetograms to those from the side camera. As the side camera also measures the linear polarizations, the 720-second magnetograms are not simply equivalent to average of 1645-second magnetograms. Instead, only one third of the time is spent measuring the circular polarizations.

2.1. Algorithm

The HMI line-of-sight magnetograms are the difference of the Doppler velocities derived from the filtergrams of the LCP and RCP measured at six wavelengths spanning the spectral line Fe I 6173 Å. Each filtergram has been corrected by removing cosmic-ray hits, filling data gaps, and correcting optical distortion. For 45-second magnetograms, the filtergrams of the LCP and RCP take into account solar rotation and are interpolated to the target time before combining them to produce the Dopplergrams. The temporal interpolation typically uses six points: whenever possible, three times before and three times after the target time. Thus filtergrams in a temporal interval of 6×45 seconds are used. A weight is applied to each filtergram that varies depending on how close the filtergram is in time to the target time. The velocity algorithm is applied separately to LCP and RCP. For the 720-second magnetograms, a temporal average is performed on the registered filtergrams before calculating the Doppler velocities. This average needs extra filtergrams before and after the nominal 720-second temporal window because the filtergrams need to be interpolated onto a regular and finer grid before averaging. The averaging uses a cosine-apodized boxcar with a Full Width Half Maximum (FWHM) of 720 seconds. The tapered temporal window used is actually 1215 seconds. Each filtergram is also de-rotated to the target time and spatially interpolated to a common solar disk center and radius that are averages from the filtergrams used to produce the Stokes vector at the target time. Finally, the velocity algorithm is applied separately to LCP and RCP. In practice, all of the processes are actually combined together in order to minimize the number of interpolations applied to the data.

The method used to derive the HMI observables, including the line-of-sight magnetograms, is described in detail by Couvidat *et al.* (2012b). Here we summarize briefly how to compute the magnetograms. The Doppler velocities and line-of-sight magnetic fields are calculated from the six wavelengths and two polarizations with the so-called MDI-like algorithm. A discrete estimate of the first Fourier coefficients of the Fe I profile is computed. The velocities are obtained by determining the arctangent of the phases of these Fourier coefficients. These velocities are then corrected for instrumental and other systematic effects using derived look-up tables. This correction is needed because the six filter transmission profiles are not δ-functions, the discrete estimate of the Fourier coefficients is not perfect (there are only six tuning positions), and the equation applied to convert the Fourier coefficients into Doppler velocities assumes that the solar line has a Gaussian profile. The look-up tables vary with the pixel location on the HMI CCDs and are based on HMI sampling-position profiles derived from calibration sequences and on realistic profiles of the solar Fe I line. The derived Doppler velocity is further adjusted by the orbital velocity that is precisely known. The difference of the LCP and RCP Doppler velocities is then used to determine the line-of-sight magnetic fields. In contrast, MDI used a single look-up table and the velocities were computed and subtracted onboard the spacecraft.

2.2. Estimate of the Magnetic Noise Level

Following the method used for MDI magnetograms (Liu, Zhao, and Hoeksema, 2004), we roughly estimate the noise levels of HMI line-of-sight magnetograms. We assume that the noise in the magnetograms has a Gaussian distribution and use a Gaussian function to fit the distribution of the low-field pixels of the magnetograms. The asterisks in Figure 1 indicate the distributions of the on-disk pixel values of a 45-second magnetogram from the front camera (left) and a 720-second magnetogram from the side camera (right) *versus* magnetic field. Only pixels within ± 200 Mx cm^{-2} within 0.95 solar radius are selected. The number

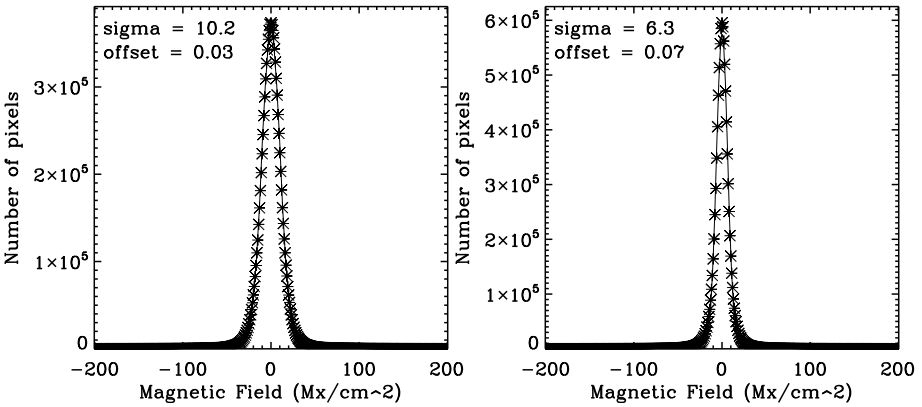

Figure 1 Estimate of the noise level for the line-of-sight magnetograms. Left: The asterisks show the distribution of the low-field pixels from a HMI 45-second magnetogram over the Sun's disk. The solid line is a Gaussian function that fits the distribution. The width (standard deviation) of the Gaussian is 10.2 Mx cm^{-2}, and the shift of the Gaussian peak is 0.03 Mx cm^{-2}. Right: Same as that in the left panel, but for a HMI 720-second magnetogram. The σ is 6.3 Mx cm^{-2} and the shift of the Gaussian peak is 0.07 Mx cm^{-2}. The width of the peak reflects both the distribution of weak field regions on the Sun and the noise in the measurement.

of pixels selected is about ten million. The solid lines are the Gaussian functions that fit the distributions. The noise levels, taken to be the σ (the standard deviation) of the best-fit Gaussian, are 10.2 Mx cm^{-2} for the 45-second magnetogram and 6.3 Mx cm^{-2} for the 720-second magnetogram. As a comparison, by using the same method, the noise is 26.4 Mx cm^{-2} and 16.0 Mx cm^{-2} for the recently calibrated (described in Section 3) MDI one-minute and five-minute magnetograms, respectively. The noise is overestimated, of course, because this distribution includes observations of real solar weak-field regions. Perhaps this is why the noise of 45-second magnetograms is not equal to 2.48 times the noise of 720-second magnetograms. The factor 2.48 is obtained by taking into account the weighted 1615-second measurements for 720-second magnetograms and 270-second measurements for 45-second magnetograms.

Noise over the Sun's disk is also estimated. Taken in June – August 2010, Figure 2 shows distributions of magnetic noise over Sun's disk derived from 11 520 45-second magnetograms at a cadence of 720 seconds (left), and from 10 800 720-second magnetograms at a cadence of 720 seconds (right). The noise at each pixel is taken to be the σ of a Gaussian function that fits the distribution of the low-field pixels from those 11 520 measurements (for 45-second magnetograms) and 10 800 measurements (for 720-second magnetograms). Note that the color bars are different in order to show comparable detail in the two images. The noise appears to be fairly symmetrical with respect to the disk center, and, as expected, gradually increases towards the limb. The horizontal-stripe patterns in the plots indicate that the noise derived using this method also includes magnetic-field signals. It gives an upper limit of noise level. The median of the noise is 10.3 Mx cm^{-2} for the 45-second magnetograms, and 6.4 Mx cm^{-2} for the 720-second magnetograms.

Dependence of noise on center-to-limb distance is also estimated. Plotted in Figure 3 are averages of the noise over azimuth as a function of distance from the disk center for the 45-second (crosses) and 720-second magnetograms (asterisks). Averaging is done over each annulus with a width of 0.1 solar radii. A second-degree polynomial that fits the data (solid lines) yields $y = 8.5 + 1.1x + 3.1x^2$for 45-second magnetograms, and

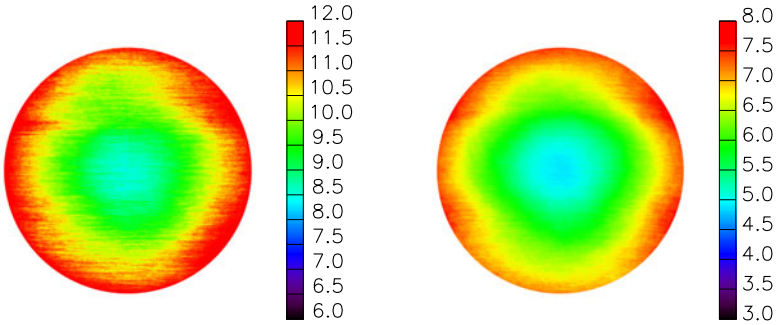

Figure 2 Distribution of noise in the line-of-sight magnetic field over Sun's disk derived from 11 520 HMI 45-second magnetograms at a cadence of 720 seconds taken in June – August 2010 (left), and from 10 800 HMI 720-second magnetograms at a cadence of 720 seconds taken in June – August 2010 (right). The median of the noise is 10.3 Mx cm^{-2} for the 45-second magnetograms, and 6.4 Mx cm^{-2} for the 720-second magnetograms. Note that the color bars are different in order to show comparable detail in the two images.

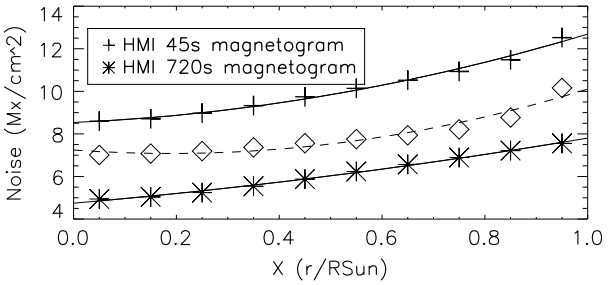

Figure 3 Dependence of noise and the center-to-limb distance for HMI 45-second (crosses) and 720-second magnetograms (asterisks), respectively. y-axis represents average of the noise over each annulus in the noise maps in Figure 2. The width of the annulus is 0.1 solar radius. x-axis refers to the distance of the middle of the annulus to the disk center [r] scaled by the Sun's radius [$R_\odot$]. A second-degree polynomial that fits the data (the solid curves) yields $y = 8.5 + 1.1x + 3.1x^2$ for 45-second magnetograms, and $y = 4.8 + 2.1x + 1.0x^2$ for 720-second magnetograms. An estimate of noise level of 45-second magnetograms from photon noise using a Monte Carlo experiment is shown in diamonds. A second-degree polynomial that fits the data (dashed line) is $y = 7.2 - 1.7x + 4.6x^2$.

$y = 4.8 + 2.1x + 1.0x^2$ for 720-second magnetograms. Here, the distance [x] is normalized by the solar radius [$R_\odot$]. This center-to-limb noise variation computed by this method may also partly come from the real signal of magnetic field: when closer to the limb, more real line-of-sight field is included in the 200 gauss limit which is used to fit the Gaussian distribution. Thus the σ of the fitted Gaussian is greater than real noise. A Monte Carlo test is performed here to further examine photon noise in HMI measurement. In this test, photon noise is added to the filtergrams that produce the 45-second magnetogram at 19:12:00 UT 2 August 2010. 2000 experiments are carried out. The standard deviation of this 2000-experiment is 7.2 Mx cm^{-2} at the disk center and increases toward the limb. This standard deviation can be deemed to be an estimate of noise level in the magnetograms mainly from photon noise. The diamonds in Figure 3 are averages of this noise over azimuth as a function of distance from the disk center, and the dashed line is a second-degree polynomial ($y = 7.2 - 1.7x + 4.6x^2$) that fits the data. It cannot reproduce the curve of the noise *versus* center-to-limb distance for the 45-second magnetograms, implying that photon noise is not

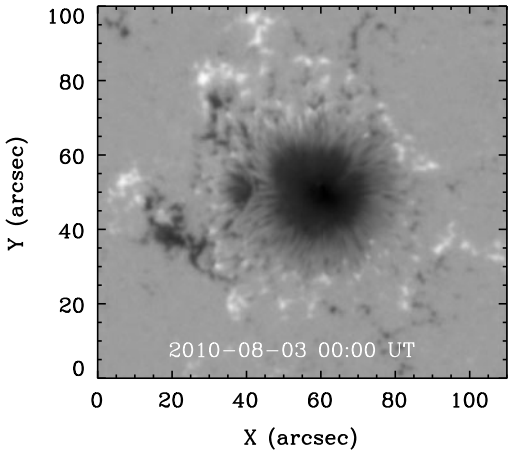

Figure 4 A HMI 720-second magnetogram taken by the side camera at 00:00 UT on 3 August 2010 for the active region AR 11092. The region was at N16W04. Pixels are 0.5 arcseconds.

the only source for the variation in distribution in the line-of-sight magnetograms. It may give a lower limit of noise level for 45-second magnetograms, however.

2.3. Periodicities

Diurnal and semi-diurnal variations are observed in strong HMI magnetic fields and probably result from the 24-hour periodicity in the orbital velocity combined with uncertainties in instrument calibration. The orbital velocity of the geosynchronous satellite relative to the Sun ranges from -3.2 km s^{-1} to 3.2 km s^{-1} from local dawn to dusk. This velocity is used to adjust the calibration curve. For velocity beyond this range, adjustment is done by extrapolating this curve. When the magnetic field is strong enough, the Zeeman effect coupled with solar rotation adds an extra shift that moves the spectral line profile (either the LCP or RCP) away from the well-determined part of the calibration curve every 24 hours. Doppler velocities derived from the extrapolated part of the calibration curve are less accurate than those computed from within the orbital velocity range. The corresponding inaccuracy in line-of-sight magnetic fields is probably the cause of the 12-hour and 24-hour periodicities, and a better calibration curve might minimize the effect. The effort to improve the calibration is ongoing. Saturation of the strongest fields might also contribute to the observed periodicities. A simulation with HMI filter transmission profiles and velocity algorithm indicates that, for a disk-center field greater than 3200 G, the uncompensated HMI measurements become saturated every 12 hours when the satellite reaches its maximum radial velocity. Further investigation is needed.

We illustrate this periodicity by analyzing the line-of-sight magnetic field in active region AR 11092 (see Figure 4). Shown in the top panel of Figure 5 is the mean unsigned magnetic field for a fixed-size patch enclosing AR 11092. Pixels greater than 600 Mx cm^{-2} are selected in order to examine periodicity in strong field only. The value 600 Mx cm^{-2} is arbitrarily chosen. The data are the 720-second magnetograms running from 30 July to 6 August 2010. The dashed curve is a third-degree polynomial that fits the mean field. The middle panel plots the difference between the mean field and the polynomial. The power spectrum of this difference is shown in the bottom panel. The 24-hour and 12-hour periodicities are clearly seen. Variation due to the periodicities is about 2.7 % of the signal on average.

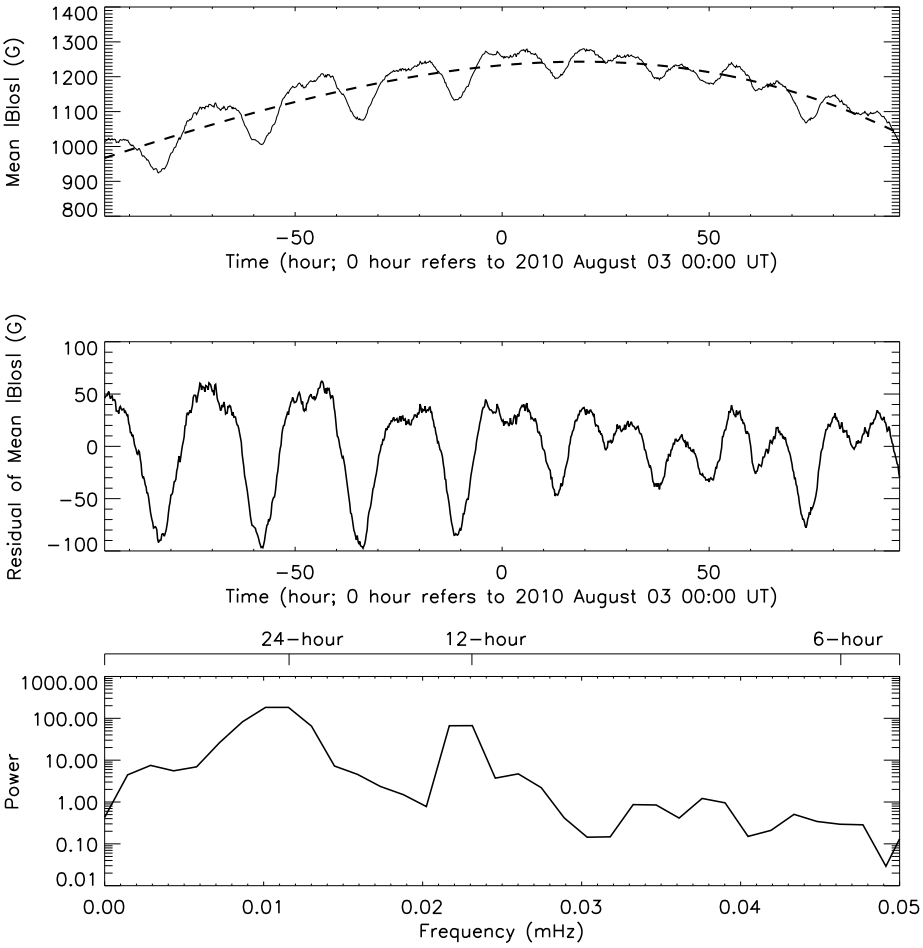

Figure 5 Top panel: The temporal profile of the mean unsigned field of AR 11092 (solid line), over–plotted by a third-degree polynomial that fits the data (dashed line). Pixels with unsigned field greater than 600 Mx cm^{-2} are chosen to compute the mean field in order to examine periodicity in strong field. 600 Mx cm^{-2} is arbitrarily selected here. Middle panel: residual of the mean unsigned field, *i.e.* the difference between the mean unsigned field and the fitted polynomial shown by the dashed line in the top panel. Bottom panel: Power spectrum of the residual of the unsigned field (in the middle panel). The observation runs eight days, from 30 July to 6 August. 24-hour and 12-hour periodicities are clearly seen. The variation due to the periodicities is about 2.7 % of the signal on average.

We also search for periodicity in quiet Sun where the Zeeman splitting is not very big. Shown in the top panel of Figure 6 are 22-day temporal profiles of the mean unsigned field in five fixed quiet-Sun areas on the solar disk. Each area encloses 80×80 pixels and includes no active regions, centered at the disk center (black), latitude $\pm 55°$ in the North and South hemispheres near the central meridian (red and pink), and longitude $\pm 55°$ East and West at the solar Equator (green and blue). The black thick line refers to the average of the mean field in the central area over the 22 days. The data are 720-second magnetograms running from 2 – 25 May 2011. The bottom panel displays the power spectra of the mean field minus

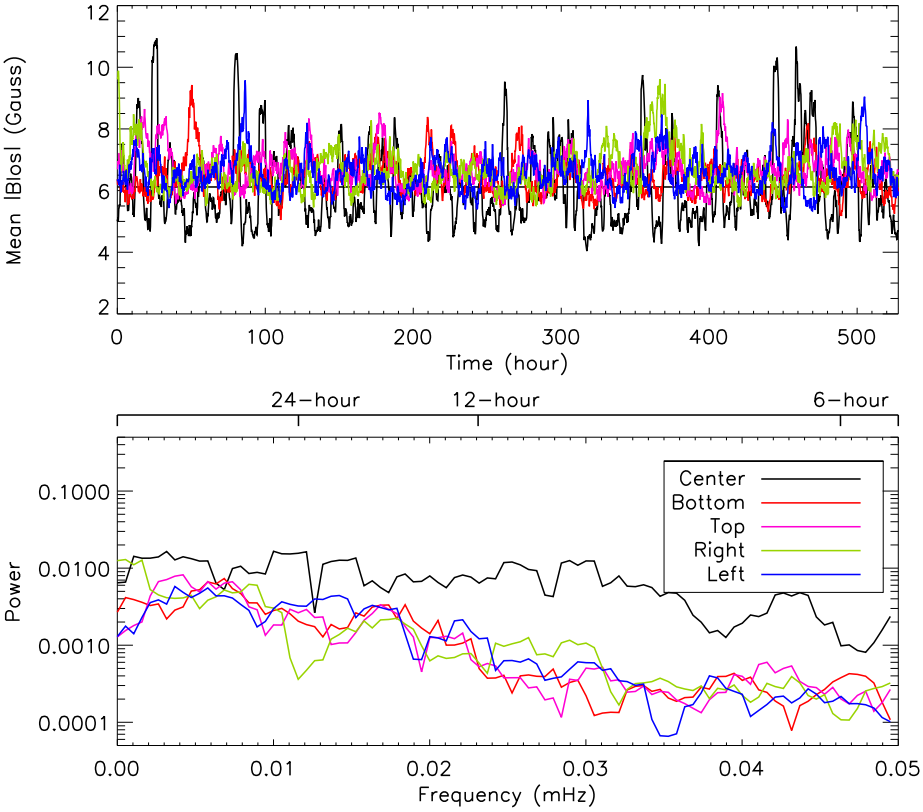

Figure 6 Periodicity in the quiet Sun in the HMI 720-second magnetograms. 22-day time profiles of the mean unsigned fields from five fixed small areas are plotted in the top panel. Each area encloses 80×80 pixels and includes no active regions. The black, red, pink, green, and blue curves refer to the mean unsigned fields from the areas centered at the disk center, latitude $\pm 55°$ at the central meridian, and longitude 55° East and West at the solar Equator, respectively. The black line denotes the average of the unsigned mean field from the central area over the 22 days. The data used were taken from 4 to 25 May 2011 with a cadence of 720 seconds. Each power spectrum in the bottom panel is computed from the unsigned mean field minus its average over the 22 days. No periodicity is seen in these power spectra.

its 22-day average. No significant periodicity is visible. This implies that the combination of the solar rotation and orbital speed alone does not introduce a significant periodicity.

3. MDI Magnetograms

This section briefly describes the MDI magnetograms and the corrections made in the past years.

3.1. Algorithm

The primary observable of MDI, the Doppler velocity, is derived from four filtergrams, $F1$–4, taken at four wavelengths equally spaced by 75 mÅ across the Ni I spectral line at

6768 Å (Scherrer *et al.*, 1995). These four filtergrams are used to compute a ratio of differences of the intensities and then this ratio is calibrated by an onboard look-up table to become a Doppler velocity. The ratio α is defined as

$$\begin{array}{ll} \alpha = (sa + sc)/sa & \text{if } sa + sc > 0, \quad \text{or,} \\ \alpha = (sa + sc)/(-sc) & \text{if } sa + sc \leq 0, \end{array} \tag{1}$$

where $sa = F1 - F3$ and $sc = F2 - F4$ (see Scherrer *et al.*, 1995 for more details). A line-of-sight magnetogram is determined using the difference of two Dopplergrams from LCP and RCP.

MDI can observe in either of two spatial resolutions. The full-disk path has a field-of-view of 34 arcminute × 34 arcminute with a pixel size of 2 arcseconds. The high-resolution path has a field-of-view of 11 arcminute × 11 arcminute slightly shifted to the North of disk center with a 0.62-arcsecond pixel size. Normally, MDI produces full-disk magnetograms at a cadence of 96 minutes. Sometimes, when high-rate telemetry is available, MDI also runs campaign programs to provide full-disk or high-resolution magnetograms with a cadence of one minute. Approximately 30 seconds are needed to obtain one magnetogram.

MDI creates two types of full-disk magnetograms in its 96-minute cadence time series. They are referred as "one-minute" and "five-minute" magnetograms in this article. A one-minute magnetogram is produced from a set of filtergrams collected during a 30-second temporal interval, as described above. A five-minute magnetogram is the average of five one-minute magnetograms obtained during a five-minute temporal interval. This unregistered average is done onboard the spacecraft.

3.2. Issues and Corrections

Listed in the following sections are issues that we identified and corrections we have made for the full-disk magnetograms. These corrections have not been applied to the high-resolution magnetograms. The corrected magnetograms are known as Level 1.8.2 magnetograms.

3.2.1. Offset

A small uncertainty in the exposure time of the camera shutter induces error in the measurements. This shutter noise adds a nearly uniform background offset to each imaged observable. An algorithm has been used to remove this offset for MDI magnetograms (Liu, Zhao, and Hoeksema, 2004). This correction is demonstrated to be effective for improving measurement and modeling of large-scale magnetic field.

The magnetic field in five-minute magnetograms is biased to the negative in the time period from March 1997 to October 2001 (see Figure 7). In this time period, MDI used a different observing frame list for deriving five-minute magnetograms, which causes this bias. It can be removed by correction for the offset (Liu, Zhao, and Hoeksema, 2004). During the years 2010 – 2011, a full-disk offset in the mean field remained after this correction.

3.2.2. Underestimation of Field Flux Density

It has been demonstrated that the MDI magnetograms underestimate the true flux density (Berger and Lites, 2003; Tran *et al.*, 2005). Berger and Lites (2003) compared a measurement of line-of-sight magnetic field taken by the *Advanced Stokes Polarimeter* (ASP) with the corresponding MDI data. The target for this comparison was a large sunspot

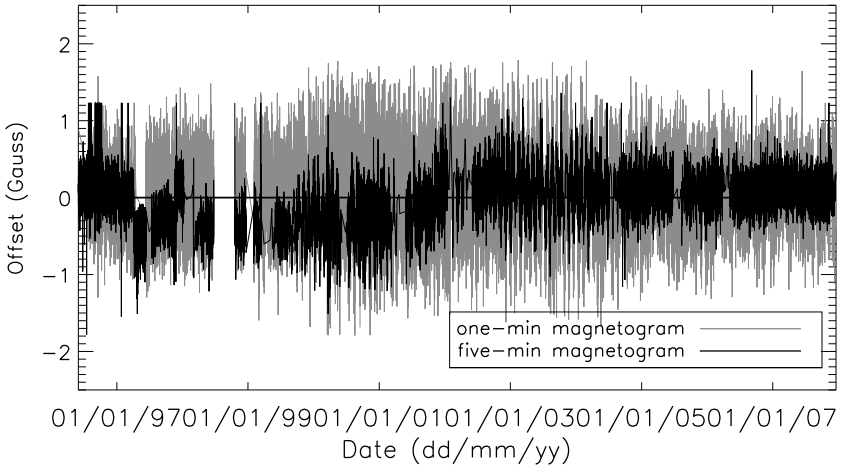

Figure 7 Computed offset of MDI magnetograms from 1996 to 2007 due to shutter noise. The dark line refers to the offset determined from five-minute magnetograms, while the gray line shows the offset from one-minute magnetograms.

group, AR 8218, at S20W22 on 13 May 1998. They found that MDI data flux-density values are lower than the data from ASP by a factor of 0.64 in the active-region plage and 0.69 in the penumbra and umbra. Tran *et al.* (2005) addressed this question in weaker-field regions by comparing the full-disk magnetograms taken by MDI and the magnetograph at Mount Wilson Observatory (MWO). Using simultaneous measurements of line-of-sight magnetic field taken at MWO in the magnetically sensitive spectral lines Fe I 5250 Å and Ni I 6768 Å (MDI spectral line), they performed a comprehensive analysis to cross-correlate the MWO magnetograms at Fe I 5250 with the corresponding MDI magnetograms. The MWO Fe I 5250 magnetograms are corrected for line-profile saturation using a factor $[\delta^{-1} = 4.5 - 2.5 \times (1 - \cos^2 \rho)]$ where ρ is the center-to-limb angle (Ulrich, 1992; Wang and Sheeley, 1995). This correction factor has been recently modified to be $\delta^{-1} = 4.15 - 2.82 \times (1 - \cos^2 \rho)$ (Ulrich *et al.*, 2009). The data used in that work were collected from March 1997 to August 2002. Ultimately they derived a ratio diagram between the MWO Fe I 5250 magnetograms and the MDI magnetograms that varies over the Sun's disk. This ratio, combined with the new saturation factor from Ulrich *et al.* (2009), is consistent with Berger and Lites' result (Ulrich *et al.*, 2009). The ratio actually used for correcting MDI full-disk magnetograms is a smoothed mask derived from the ratio diagram shown in Figure 6 of Tran *et al.* (2005) after being corrected by the new saturation factor of Ulrich *et al.* (2009). Such a smoothness is necessary to avoid artificial discontinuities that the calibration may introduce. Shown in the left panel of Figure 8 is the distribution of the ratio over the Sun's disk. The average of this ratio over each annulus is plotted in the right panel. The width of the annulus is 0.02 solar radii. The ratio shows a sharp decrease towards the limb.

3.2.3. Non-Uniform Noise over the Disk

Noise in MDI magnetograms is not uniform over the disk due to different optical distortions in the left- and right-circular analyzers that allow granulation and *p*-mode oscillations to leak in as noise. Because the filtergrams are combined onboard, the distortions cannot be fixed in the MDI data. The lower-right part of the CCD is noisier. The noise, estimated from

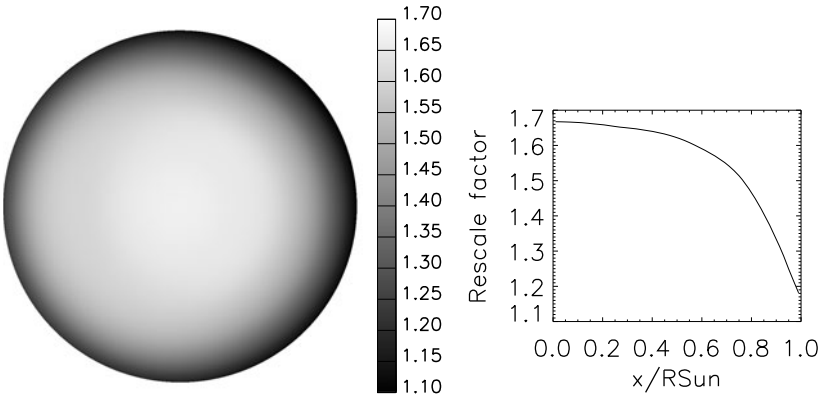

Figure 8 Left: Smoothed rescaling factor applied to the MDI magnetograms. Right: Azimuthal average of the rescaling factor as a function of the distance from disk center, scaled by the Sun's radius [$R_\odot$].

Figure 9 Distribution of magnetic noise over Sun's disk derived from about 32 000 calibrated MDI one-minute magnetograms taken in March 2007 in a campaign program. MDI took one magnetogram every one minute in this program. The bottom right area is noisier. The median is 26.4 Mx cm^{-2}.

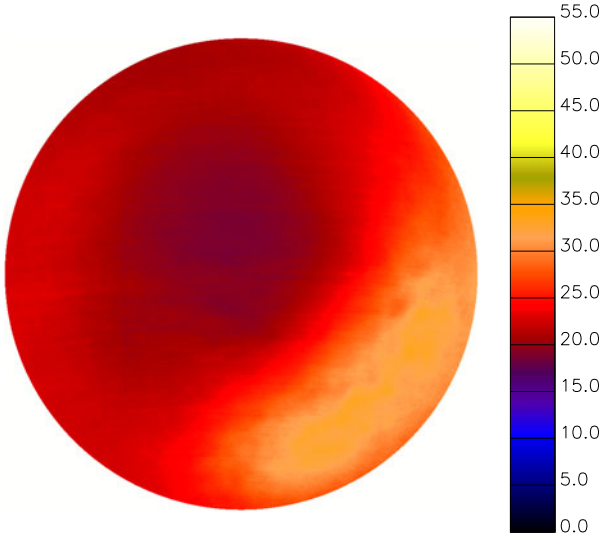

one month of data using a Gaussian function to fit the distribution of low-flux-density pixels as illustrated by Liu, Zhao, and Hoeksema (2004), is 24.7 Mx cm^{-2} and 28.9 Mx cm^{-2} for the left and right half of the image for one-minute magnetograms, and 14.9 Mx cm^{-2} and 17.4 Mx cm^{-2} for five-minute magnetograms. Usually the noise appears higher in the southwest part of magnetograms. Since 2003, about half of the MDI images are upside down due to the orientation of the SOHO spacecraft. The noisy part of the disk in these data is the Northeast.

Figure 9 shows the noise over the Sun's disk derived from about 32 000 one-minute magnetograms taken in March 2007 during an MDI dynamics program, in which MDI takes full-disk magnetograms every minute (usually MDI takes one full-disk magnetogram every 96 minutes). For each pixel, we use a Gaussian function to fit distribution of the low-field pixels of the 32 000 measurements. Figure 9 displays the width (standard deviation) of the

Gaussian function. It increases from disk center to the limb. It is highest in the bottom right area. The median is 26.4 Mx cm^{-2}.

3.2.4. Saturation

Low intensity in sunspot umbrae and limitations of the 15-bit onboard numerical precision lead to saturation seen in some sunspot umbrae in the MDI magnetograms (Liu, Norton, and Scherrer, 2007). Since MDI intensity data are also available at a lower cadence, it might be possible to correct the saturation in the magnetograms using the well-established relationship between the continuum intensity and the magnetic field strength (*I–B* relationship) (*e.g.* Kopp and Rabin, 1992; Martínez Pillet and Vázquez, 1993).

3.2.5. Magnetic Field Reversal during Some Major Flares

Sometimes the magnetic field appears to reverse in MDI magnetograms during major flares. This reversal is temporary, only observed during flares. Usually the reversal develops the same patterns as the flare bright ribbons. It is unlikely to be a real change of the magnetic field. Qiu and Gary (2003) suggested that the spectral line Ni I 6768 Å switches from absorption into emission during major flares, causing the apparent reversal. Using HMI observations, however, Martínez Oliveros *et al.* (2011) found that the photospheric spectral line Fe I 6173 Å that HMI uses remains in absorption during a white-light flare, although it shifts greatly in wavelength to the blue. The reason causing this reversal is still not clear. So far, we have no method to correct for this effect.

4. Comparison of HMI and MDI Magnetic Field Observations

4.1. Comparison of HMI and MDI Magnetograms

4.1.1. Magnetic Flux Density in HMI and MDI Magnetograms

HMI and newly calibrated MDI magnetograms are compared on a pixel-by-pixel basis. The method is described below. We first reduce HMI spatial resolution to be comparable to MDI's by convolving a two-dimensional Gaussian function. The Gaussian function used has a FWHM of 4.7 HMI pixels, and is truncated by 15 HMI pixels. The reason to choose this FWHM is described in next paragraph. We then map each two-arcsecond MDI pixel onto the solar surface. We average the HMI pixels enclosed in this area from the corresponding blurred HMI magnetogram. HMI pixels that are only partly included in the area are adjusted by this fraction. In this way, we generate a MDI proxy pixel. Putting these proxy pixels together, we obtain a MDI proxy magnetogram. For each MDI magnetogram, we corrected distortion, and also corrected for an offset of the position angle [P-angle]. C. Toner (private communications, 2004) estimated the P-angle offset by intercomparing MDI and GONG images, and observations taken during the 1999 November transit of Mercury in front of the Sun (see Korzennik, Rabello-Soares, and Schou, 2004). He found the offset is $0.19 \pm 0.04°$, and $0.20 \pm 0.05°$, respectively. Korzennik, Rabello-Soares, and Schou (2004) found a P-angle offset of 0.25°. Here we take 0.22° (clockwise), an average of them, as the P-angle offset for MDI magnetograms. Using the P-angle offset corrected MDI magnetograms as references, we determine rotation angles that may need to be applied to the HMI magnetograms by computing the correlation coefficient between the MDI magnetograms and the

proxy MDI magnetograms from the rotated HMI magnetograms, as described above. The range of the rotation angles explored is from -1° to $+1^\circ$ with a step of 0.05°. The correlation coefficient reaches its maximum when the HMI 45-second magnetograms rotate 0.05° (clockwise) and when the HMI 720-second magnetograms rotate 0.10°, respectively. These angles are therefore applied to the HMI magnetograms for comparison. Since the rotation angles determined above are well within the error of the MDI P-angle offset, they are not deemed to be the P-angle offsets for the HMI front and side cameras. More sophisticated methods are needed to precisely determine the offsets.

We carried out two tests to select an optimal FWHM for the Gaussian function that is applied to HMI magnetograms to produce the most comparable MDI proxy magnetograms. The first method is to compute the Pearson correlation coefficient and Spearman rank order between MDI pixels and MDI proxy pixels from the HMI magnetograms. The HMI magnetograms are blurred by the Gaussian function with various FWHM before generating MDI proxy pixels. The pixels used are within $0.5R_\odot$ of Sun center to avoid possible misalignment near the limb. $R_\odot$ is the Sun's radius. The range of FWHM explored is from 4.0 to 6.0 HMI pixels with a step of 0.1 HMI pixels. The comparison without blurring HMI magnetograms is also examined here. The Pearson coefficient and Spearman rank order reach the maximum when FWHM equals 4.3 and 5.1, respectively. The second method is suggested by J. Harvey (private communication, 2012) when comparing HMI and SOLIS magnetograms. In this method, we assumed various scaling factors and subtracted MDI magnetograms from the scaled MDI proxy magnetograms. The results (difference-images) are then examined by calculating root mean square (RMS) over the disk. Two free parameters are determined using this method: FWHM of the Gaussian function and a scaling factor applied to MDI proxy magnetograms. RMS reaches minimum when FWHM $= 4.5$ and scaling factor equals 1.4. Averaging the results above yields FWHM $= 4.7$ HMI pixels, which is thus chosen in this work.

Plotted in the top panel of Figure 10 is a scatter plot of the MDI pixels and the MDI proxy pixels from 12 pairs of HMI 45-second magnetograms and MDI one-minute magnetograms taken in June – August 2010. Each pair of magnetograms was taken at the same time. MDI magnetograms are carefully examined to ensure that data used do not contain obvious saturated pixels in sunspots. Pixels within $0.866R_\odot$ of Sun's center (roughly $\rho < 60^\circ$, where ρ is center-to-limb angle) are selected for this comparison. The background image represents the log density of the scatter points. The white line refers to a linear function that fits the data. It is MDI $= -0.18 + 1.40 \times$ HMI. The errors of the slope and intercept are too small to be given here. The middle panel shows a similar scatter plot of the MDI and MDI proxy pixels from 12 pairs of MDI and HMI 720-second magnetograms. The slopes of the linear fit between the HMI and MDI magnetograms imply that the line-of-sight pixel-averaged magnetic signal inferred from MDI data is greater than that derived from the HMI data by a factor of 1.40. There is also a zero-point offset between them: the MDI magnetograms appear to be shifted slightly towards the negative. In the bottom panel is a scatter plot between the 12 pairs of the HMI 45-second and 720-second magnetograms with a two-arcsecond pixel size. This indicates that the HMI 45-second and 720-second magnetograms match very well.

Figure 10 appears to suggest that the scale factor might be smaller for strong fields. Fitting weak-field and strong-field pixels separately with a linear function is thus tested. The slope for strong fields is lower than that for weak fields by about 10 %. The value chosen to separate strong field and weak field is 600 Mx cm^{-2}, and pixels used here are within $0.866R_\odot$ of Sun center. The results are summarized in Table 1. The parameters a and b are coefficients of a linear fit that is MDI $= a + b \times$ HMI. The errors of those coefficients are close to zero, and thus not given in this table. cc is the Pearson correlation coefficient.

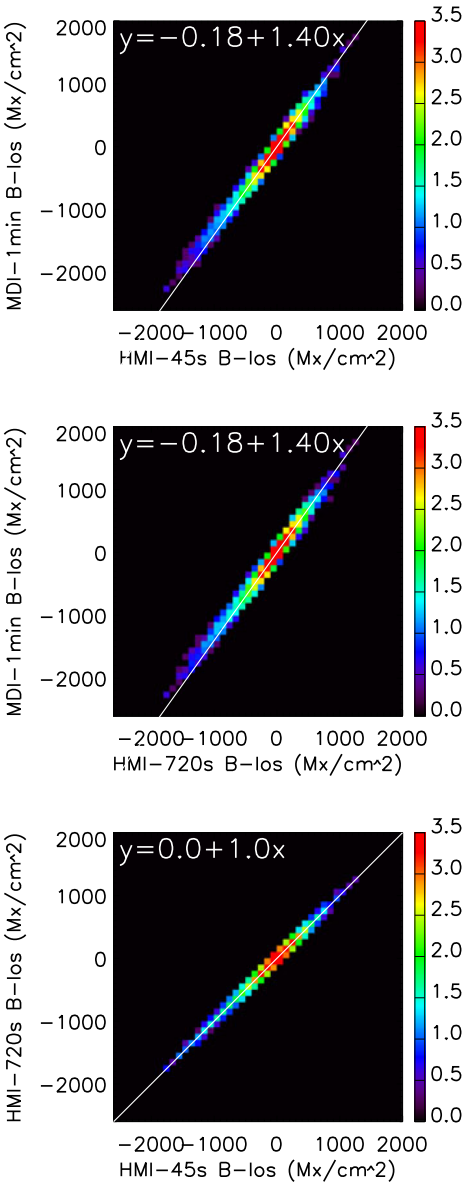

Figure 10 Comparison of HMI and MDI magnetograms. The HMI magnetograms are used to emulate the MDI magnetograms (see the text for more detail). From top to bottom are the scatter plots between 12 pairs of the MDI one-minute magnetograms and the emulated MDI magnetograms from the HMI 45-second magnetograms (top), from the HMI 720-second magnetograms (middle), and the HMI 45-second and 720-second magnetograms (bottom). The background images represent the log density of the scatter points. The white lines refer to linear functions that fit the data. The data were taken in June – August 2010.

Comparison is also done for different areas on the Sun's disk. Shown from top to bottom in Figure 11 are the scatter plots for the pixels within $0° < \rho < 30°$, $30° < \rho < 45°$, and $45° < \rho < 70°$, where ρ is the center-to-limb angle. The data used are the same as in Figure 10. Again, the images represent the log density of the scatter points, and the white lines refer to linear functions that fit the scatter points. The panels in the left column are comparisons between HMI 45-second and MDI magnetograms, and in the right between HMI 720-second and MDI magnetograms. The slopes for these three areas are 1.43, 1.40, and 1.26, respectively. This center-to-limb variation is very much similar to that of the MDI

Table 1 Summary of comparisons between HMI 45-second and MDI one-minute magnetograms, and between HMI 720-second and MDI one-minute magnetograms. The first column refers to the area where the pixels are used for the comparison. ρ is the center-to-limb angle. The second column denotes which magnetograms are compared. The third column denotes which pixels are selected for the comparison. *weak field* and *strong field* refer to weak- and strong-field pixels, and *all* means all pixels. Weak- and strong-field pixels are separated by 600 Mx cm^{-2}. The parameters a, b, and cc in the following columns are coefficients of a linear fit that is MDI $= a + b \times$ HMI, and Pearson correlation coefficient, respectively. The errors for a and b are very small, and thus not given here.

Area	Comparison	Pixels	a	b	cc
$0° < \rho < 60°$	MDI *vs.* HMI 45-s	all	−0.18	1.40	0.82
	MDI *vs.* HMI 720-s	all	−0.18	1.40	0.82
	MDI *vs.* HMI 45-s	weak-field	−0.18	1.44	0.79
	MDI *vs.* HMI 720-s	weak-field	−0.18	1.44	0.79
	MDI *vs.* HMI 45-s	strong-field	9.34	1.31	1.00
	MDI *vs.* HMI 720-s	strong-field	10.2	1.31	1.00

Table 2 Same as in Table 1 but for different areas. Comparisons between MDI and HMI 720-second magnetograms are the same as between MDI and HMI 45-second magnetograms, and thus are not listed here.

Area	Comparison	Pixels	a	b	cc
$0° < \rho < 30°$	MDI *vs.* HMI 45-s	all	−0.13	1.43	0.90
	MDI *vs.* HMI 45-s	weak-field	−0.13	1.47	0.87
	MDI *vs.* HMI 45-s	strong-field	15.9	1.35	1.00
$30° < \rho < 45°$	MDI *vs.* HMI 45-s	all	−0.16	1.40	0.80
	MDI *vs.* HMI 45-s	weak-field	−0.17	1.43	0.77
	MDI *vs.* HMI 45-s	strong-field	16.5	1.32	1.00
$45° < \rho < 70°$	MDI *vs.* HMI 45-s	all	−0.21	1.26	0.51
	MDI *vs.* HMI 45-s	weak-field	−0.21	1.27	0.50
	MDI *vs.* HMI 45-s	strong-field	−19.7	1.10	0.99

rescaling factor (see Figure 8) that has been used to calibrate the MDI magnetograms. We also fit strong-field and weak-field pixels separately. The slopes for strong-field comparison are again lower than those for weak field by about 10 %. The results are summarized in Table 2. Since comparisons between MDI and HMI 720-second magnetograms are the same as those between MDI and HMI 45-second magnetograms, they are not listed in the table. Low cc in limb areas implies that alignment between two images is not perfectly done near the limb. Use of the slope in this area needs caution.

4.1.2. Some Examinations for Quality of HMI and MDI Magnetograms

Figure 12 shows the power spectra of HMI eight-hour 45-second magnetograms (left) and MDI high-resolution magnetic field data (right). The data were taken on 29 March 2010. The power spectra were made from a quiet area near the disk center. The ridges in the MDI spectral map indicate significant p-mode leakage into the magnetograms. It is probably due to the different optical distortions in the left- and right-circular analyzers that leak the gran-

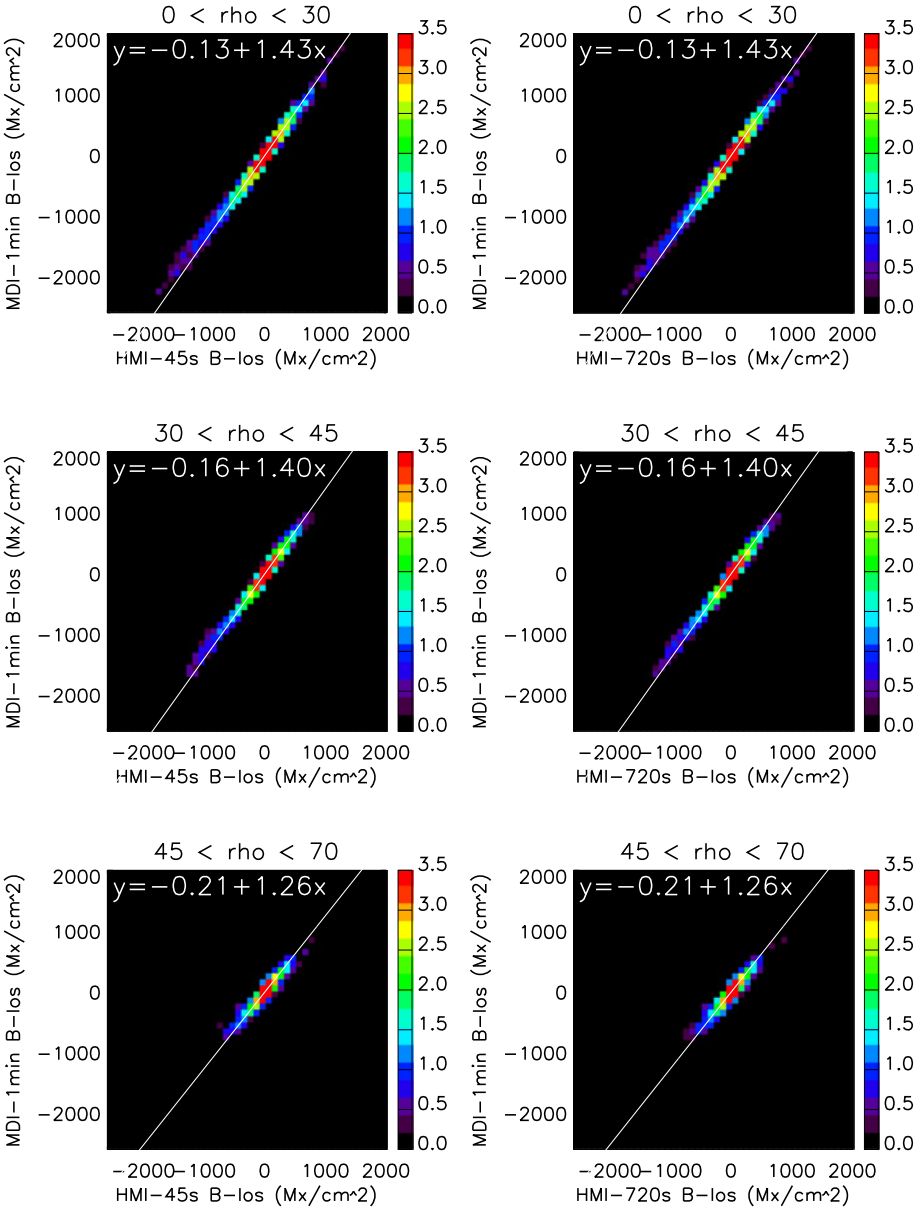

Figure 11 The same as in Figure 10 but done for different areas on Sun's disk. From top to bottom are scatter plots of the pixels within $0° < \rho < 30°$, $30° < \rho < 45°$, and $45° < \rho < 70°$, respectively. ρ is the center-to-limb angle. The panels in the left column are the comparison between HMI 45-second and MDI magnetograms, and on right between HMI 720-second and MDI magnetograms. The images represent the log density of the scatter points.

ulation signal and *p*-modes into the magnetograms, as discussed in Section 3. This leakage problem has been fixed with the HMI instrument: no *p*-mode ridges are found in the power spectrum of the HMI magnetic-field data.

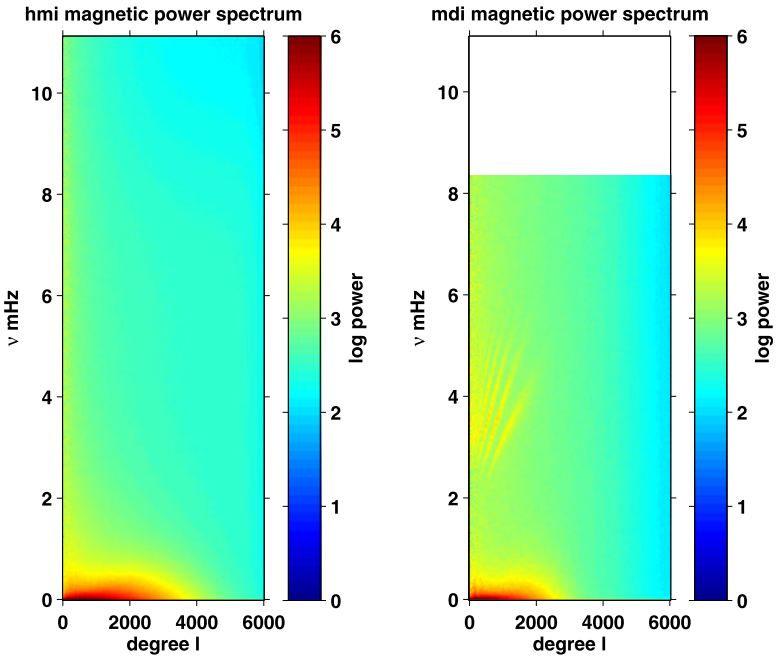

Figure 12 The power spectrum of eight-hour 45-second HMI magnetic-field data (left) and eight-hour MDI high-resolution magnetic-field data (right) near the solar disk center. The ridges can be clearly seen in the MDI spectrum, indicating significant leakage of the *p*-mode into the MDI magnetograms. No *p*-mode ridges are seen in the HMI spectrum.

The quality of data towards the solar limb is also examined. Figure 13 shows an area of the Sun from North 60° to the North Pole from an MDI one-minute magnetogram (top), an HMI 45-second magnetogram (middle), and an HMI 720-second magnetogram (bottom). The images are all scaled to ± 40 Mx cm^{-2}. The data were taken on 11 September 2010 when the North polar region is well observed. Many small-scale magnetic elements that are not visible in the MDI magnetogram are clearly seen in the HMI magnetograms.

4.1.3. Large-scale Magnetic Field Inferred by HMI and MDI Magnetograms

Comparison of large-scale magnetic field is also done. Time-series profiles of the mean solar magnetic field are shown in Figure 14. The daily average mean field from Wilcox Solar Observatory (WSO) is measured with integrated sunlight in a mode of measuring the Sun-as-a-star and has a low zero-level error. The WSO mean field plotted here is multiplied by a factor of 1.8 for the saturation correction (Svalgaard, Duvall, and Scherrer, 1978) for the Fe I 5250 Å spectral line. The "mean field" from MDI and HMI, on the other hand, is derived from the full-disk line-of-sight magnetograms by simply summing up the magnetic field over the solar disk. It differs from the WSO mean field, because it does not take into account the solar intensity. The plot runs from June 2010 to May 2011. To better show the comparison, we do not plot the mean field from HMI 45-second magnetograms because it is very close to that from HMI 720-second magnetograms. The three measurements match well in general, but the MDI mean field shows a slight shift towards the negative, implying that there might be a systematic offset of the zero point of the magnetic field in

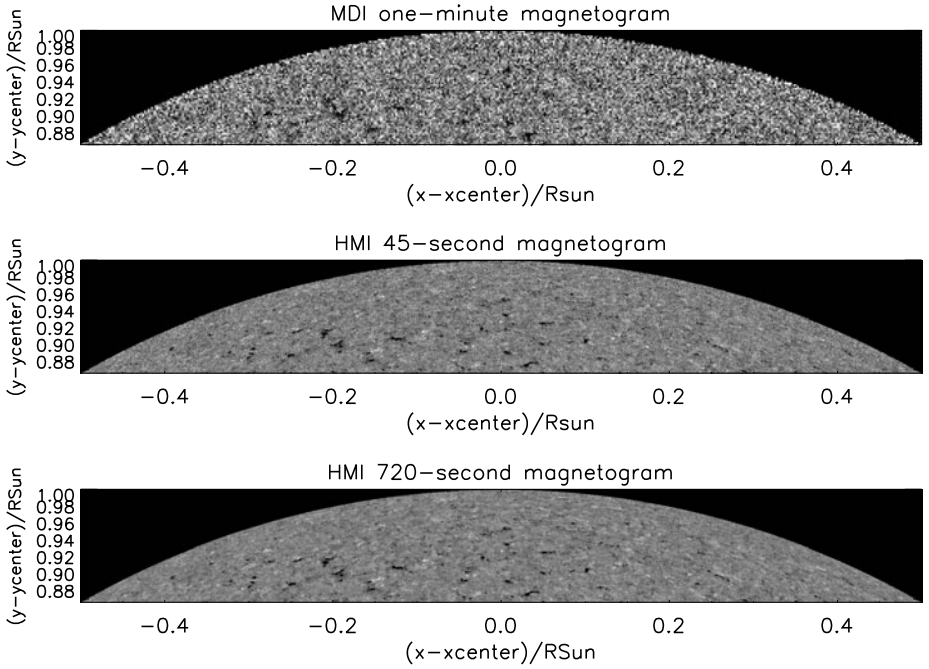

Figure 13 Solar North Pole observed by MDI and HMI on 11 September 2010. From top to bottom: MDI one-minute magnetogram, HMI 45-second magnetogram, and HMI 720-second magnetogram. The region is from North 60° to the North Pole. The images are all scaled to ± 40 Mx cm^{-2}. The B-angle was $+7.25°$. *x*-axis and *y*-axis refer to horizontal and vertical distances to the disk center, scaled by the Sun's radius [$R_\odot$]. *x*-center and *y*-center are coordinates of the disk center.

the MDI magnetograms in that time period, even though the offset of each MDI magnetogram has been corrected (Section 3.2.1). It is also interesting to see that the consensus mean field also shifts to the negative in this ten-month time period. Further investigation is needed.

4.2. Comparison of HMI and MDI Synoptic Charts

Magnetic-field synoptic charts are produced from the HMI and MDI full-disk magnetograms. The procedure is described below. Magnetograms are firstly remapped to a high-resolution Carrington coordinate grid. Then the field strength measured at each synoptic grid point is averaged from all of the contributing remapped magnetograms, after taking into account the differential rotation, to form a map of the entire solar surface. Currently the MDI average is done with the measurements from the equivalent of twenty one-minute magnetograms that contribute pixels observed closest to the central meridian. Similarly, HMI synoptic maps combine twenty 720-second magnetograms. In this way the variation of the noise over the entire map is greatly minimized, which otherwise has the potential to impact further applications. The effective temporal width of the MDI synoptic-map contribution is about one day, depending on the distribution of one- and five-minute magnetograms. HMI synoptic maps average data from about four hours at each Carrington longitude, *i.e.* within two hours of central meridian passage. This means that the pixels used for MDI maps are roughly within $\pm 7°$ of central meridian, and $\pm 1.2°$ for HMI maps. The MDI synoptic maps retain

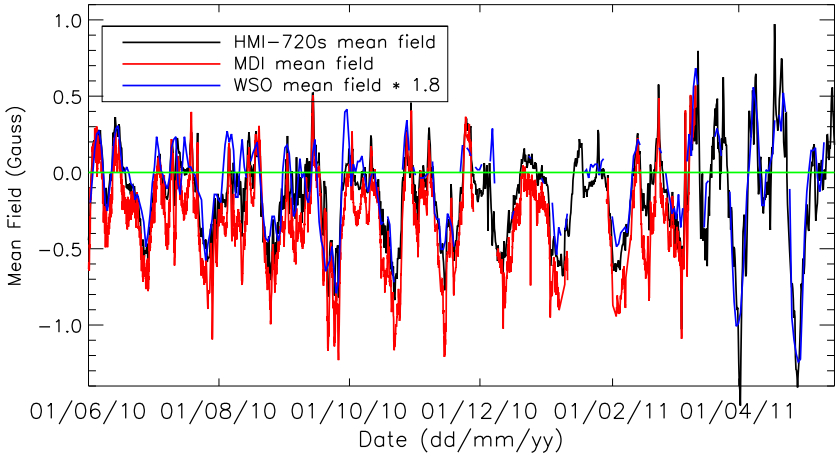

Figure 14 The mean solar magnetic field from 1 June 2010 to 15 May 2011. The black and red profiles refer to the mean fields from HMI 720-second and MDI magnetograms, respectively. The mean field from HMI 45-second magnetograms is not plotted here because it is very close to that from HMI 720-second magnetograms. The blue curve represents the daily average mean field measured at WSO, multiplied by 1.8. The "mean field" from HMI and MDI is derived by summing the line-of-sight magnetic field over the solar disk. The MDI "mean field" shifts slightly to the negative.

the disk-center resolution of the single magnetograms, which results in a 3600 × 1080-pixel map. The HMI synoptic maps have a size of 3600×1440, which indicates that the resolution is lower than the disk-center resolution of single HMI magnetograms. A two-dimensional Gaussian function is applied to HMI full-resolution remapped data to reduce the spatial resolution before generating synoptic maps. The width of the Gaussian is three pixels. The axes are linear in Carrington longitude and sine latitude. Using a Gaussian function to fit the distribution of the low-field pixels over a line-of-sight magnetic field chart yields a noise of 2.3 Mx cm^{-2} for HMI synoptic charts and 5.0 Mx cm^{-2} for MDI synoptic charts.

The variation of the noise over the synoptic charts is examined. Shown in Figure 15 are the standard deviation of the pixels within latitude $-35°$ to $+35°$ as a function of longitude for the MDI (black) and HMI (gray) line-of-sight magnetic field synoptic maps for Carrington Rotation 2100. For each column of the maps, only the weak-field pixels within ± 15 Mx cm^{-2}, three times the noise in a typical MDI synoptic map, are selected. The standard deviation [σ] of the selected pixels at each column does not change very much with longitude, suggesting that the noise is fairly uniform over the synoptic maps. The average of the σ over the longitude is 3.7 Mx cm^{-2} for the HMI chart and 5.6 Mx cm^{-2} for the MDI chart, which are greater than the noise estimated above. Magnetic-field signal in the selected pixels may account for this difference.

We also examine periodicity in the HMI synoptic maps because the strong field in the HMI magnetograms shows 24-hour and 12-hour periodicities, which may leak into the maps. Plotted in Figure 16 are the mean unsigned fields at various latitudes as a function of longitude (top), and their power spectra (bottom). The data used is the HMI synoptic chart for the Carrington Rotation 2110. The size of the map is 3600 × 1440. For each column of the map, we choose five 120-pixel segments centered at $\pm 50°$, $\pm 20°$, and the Equator. As synoptic charts are produced using the pixels near the central meridian in each magnetogram, each sunspot's pixel in a HMI synoptic chart needs data taken typically within four hours that is not enough to detect 24-hour or 12-hour periodicity. Thus we use only

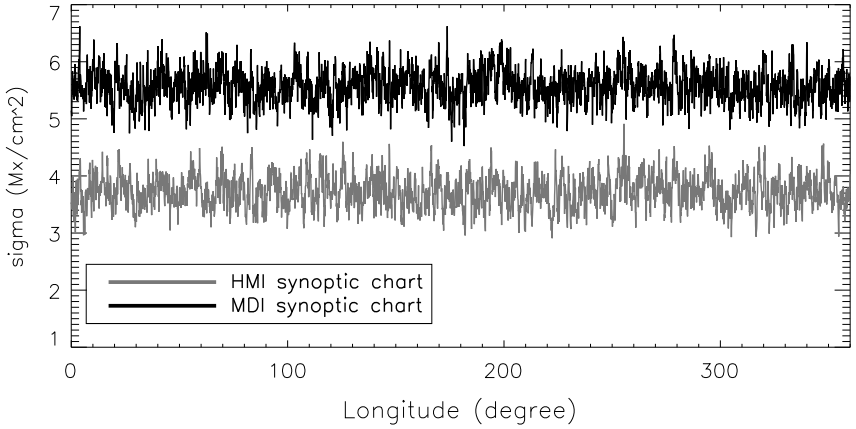

Figure 15 The standard deviation [σ] of the pixels within latitudes $\pm 35°$ in the HMI synoptic map (gray) and MDI synoptic map (black) for Carrington Rotation 2100. The pixels selected for this computation are within $\pm$ 15 Mx cm^{-2}. 15 Mx cm^{-2} is three times the noise level of a typical MDI synoptic map. It does not change very much with longitude, suggesting that the noise is fairly uniform over the synoptic maps.

weak-field pixels to search for periodicity. The mean unsigned field for each segment is computed from the pixels within ± 6.9 Mx cm^{-2}, three times the noise in a typical HMI synoptic chart. No significant periodicity is visible in the power spectra plots (the bottom panel). This is consistent with the result in Section 2.3 that no periodicity is detected in weak field in HMI magnetograms.

5. Summary

In this article, we compare the line-of-sight magnetograms obtained by HMI and MDI. A pixel-by-pixel comparison shows that the line-of-sight magnetic signal inferred from the calibrated MDI data is greater than that derived from the HMI data by a factor of 1.40. This factor varies with the distance between the area and the disk center, which is due to the spatially dependent calibration factor applied to the MDI magnetograms. Comparing strong-field and weak-field pixels separately yields slightly different scaling factors. The factor for strong fields is about 10 % lower than that for weak fields. The value used here to separate weak and strong field is 600 Mx cm^{-2}. An upper bound to the random noise for the HMI 720-second magnetograms is 6.3 Mx cm^{-2} and 10.2 Mx cm^{-2} for the 45-second magnetograms. The noise gradually increases towards the limb. The sensitivity in HMI magnetograms is much better than that in MDI magnetograms and more uniform: many small-scale magnetic elements in the polar region that are not seen in MDI magnetograms are clearly visible in HMI magnetograms. No p-mode leakage is detected in the HMI magnetograms, but it is significant in the MDI magnetograms. 12-hour and 24-hour periodicities are detected in strong fields in the HMI magnetograms.

We also briefly describe the MDI full-disk magnetograms and the corrections made for the data in the past years. The current MDI full-disk magnetograms have been corrected for the zero-point offset and underestimation of the flux density. The calibrated magnetograms are known as Level 1.8.2 MDI magnetograms. These corrections have not been applied to the MDI high-resolution magnetograms. Level 1.8.2 MDI magnetograms have a noise of 26.4 Mx cm^{-2} for the one-minute magnetograms and 16.2 Mx cm^{-2} for the five-minute

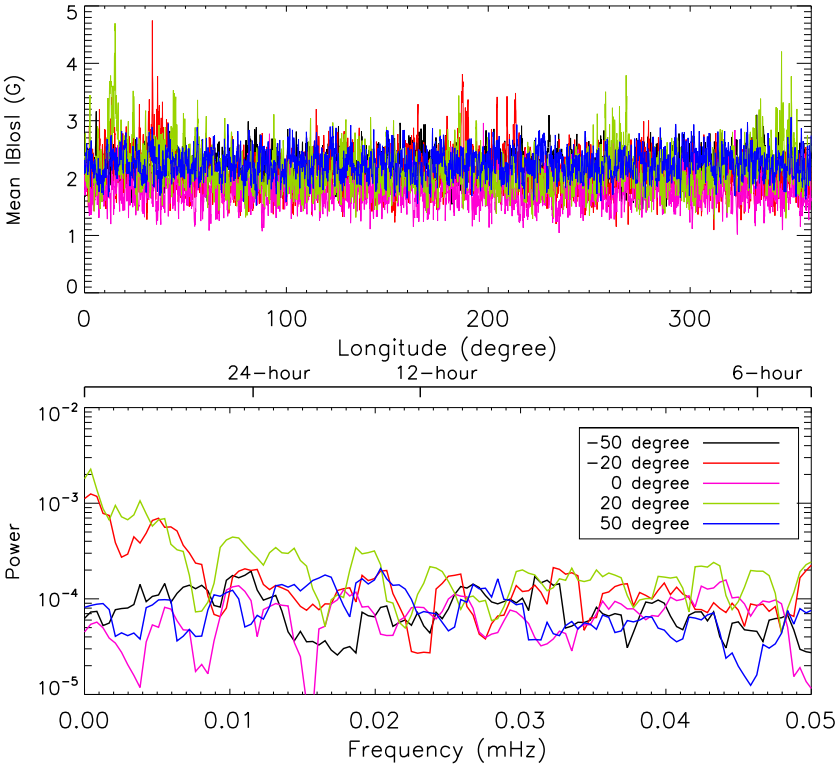

Figure 16 Top: The mean unsigned fields as a function of longitude for the HMI line-of-sight magnetic-field synoptic chart for CR 2110. The mean unsigned fields are computed from five segments centered at latitudes $\pm 50°$, $\pm 20°$, and Equator at each longitude. There are 120 pixels in each segment. The mean unsigned field is computed from the pixels within ± 6.9 Mx cm^{-2}, three times the noise level of typical HMI synoptic charts. Bottom: power spectra of those mean unsigned fields. No periodicity is seen.

magnetograms. The noise variation over the Sun's disk is likely due to the different optical distortions in the left and right circular polarization analyzers that allow the granulation and *p*-mode oscillation to leak in as noise. The bottom-right corner of MDI CCD images is noisier. Saturation sometimes seen in sunspot umbrae is caused by the low intensity and the limitation of the onboard computation. Field reversal is occasionally observed during major flares that is likely to be artificial. Recent mean magnetic-field measurements by MDI appear to be slightly shifted towards the negative. HMI filtergrams are all retrieved. So some of these effects can be eliminated.

The noise in the HMI line-of-sight field synoptic charts is 2.3 Mx cm^{-2}, compared to 5.0 Mx cm^{-2} in the MDI synoptic charts. It appears to be fairly uniform over the entire map. No weak-field periodicity is found in the HMI synoptic charts.

Acknowledgements We wish to thank the large team who have made great contributions to this SDO mission for their hard work! We thank the anonymous referee for the suggestions and comments that helped improve the article. We appreciate very much the discussions with R. Ulrich, which led to further examination of the pixel-by-pixel comparison between MDI and HMI magnetograms. This work was supported by NASA Contract NAS5-02139 (HMI) to Stanford University. The data have been used by courtesy of NASA/SDO and the HMI science team. SOHO is a project of international cooperation between ESA and NASA.

References

Berger, T.E., Lites, B.W.: 2003, *Solar Phys.* **213**, 213. doi:10.1023/A:1023953716633.

Borrero, J.M., Tomczyk, S., Kubo, M., Socas-Navarro, H., Schou, J., Couvidat, S., Bogart, R.: 2011, *Solar Phys.* **273**, 267. doi:10.1007/s11207-010-9515-6.

Couvidat, S., Schou, J., Shine, R.A., Bush, R.I., Miles, J.W., Scherrer, P.H., Rairden, R.L.: 2012a, *Solar Phys.* **275**, 285. doi:10.1007/s11207-011-9723-8.

Couvidat, S., Rajaguru, S.P., Wachter, R., Sankarasubramanian, K., Schou, J., Scherrer, P.H.: 2012b, *Solar Phys.* doi:10.1007/s11207-011-9927-y.

Kopp, G., Rabin, D.: 1992, *Solar Phys.* **141**, 253. doi:10.1007/BF00155178.

Korzennik, S.G., Rabello-Soares, M.C., Schou, J.: 2004, *Astrophys. J.* **602**, 481.

Leka, K.D., Barnes, G., Crouch, A.D., Metcalf, T.R., Gary, G.A., Jing, J., Liu, Y.: 2009, *Solar Phys.* **260**, 83. doi:10.1007/s11207-009-9440-8.

Liu, Y., Zhao, X.P., Hoeksema, J.T.: 2004, *Solar Phys.* **219**, 39. doi:10.1023/B:SOLA-0000021822-07430-d6.

Liu, Y., Norton, A.A., Scherrer, P.H.: 2007, *Solar Phys.* **241**, 185. doi:10.1007/s11207-007-0296-5.

Martínez Oliveros, J.C., Couvidat, S., Schou, J., Krucker, S., Lindsey, C., Hudson, H.S., Scherrer, P.: 2011, *Solar Phys.* **269**, 269. doi:10.1007/s11207-010-9696-z.

Martínez Pillet, V., Vázquez, M.: 1993, *Astron. Astrophys.* **270**, 494.

Metcalf, T.R., Leka, K.D., Barnes, G., Lites, B.W., Georgoulis, M.K., Pevtsov, A.A., Balasubramaniam, K.S., Gary, G.A., Jing, J., Li, J., Liu, Y., Wang, H.N., Abramenko, V., Yurchyshyn, V., Moon, Y.-J.: 2006, *Solar Phys.* **237**, 267. doi:10.1007/s11207-006-0170-x.

Norton, A.A., Pietarila Graham, J., Ulrich, R.K., Schou, J., Tomczyk, S., Liu, Y., Lites, B.W., López Ariste, A., Bush, R.I., Socas-Navarro, H., Scherrer, P.H.: 2006, *Solar Phys.* **239**, 69. doi:10.1007/s11207-006-0279-y.

Pesnell, P.D., Thompson, B.J., Chamberlin, P.C.: 2012, *Solar Phys.* **275**, 3. doi:10.1007/s11207-011-9841-3.

Qiu, J., Gary, D.E.: 2003, *Astrophys. J.* **599**, 615.

Scherrer, P.H., Bogart, R.S., Bush, R., Hoeksema, J.T., Kosovichev, A.G., Schou, J., Rosenberg, W., Springer, L., Tarbell, T.D., Title, A., Wolfson, C.J., Zayer, I., MDI Engineering Team: 1995, *Solar Phys.* **162**, 129. doi:10.1007/BF00733429.

Scherrer, P.H., Schou, J., Bush, R.I., Kosovichev, A.G., Bogart, R.S., Hoeksema, J.T., Liu, Y., Duvall, T.L. Jr., Zhao, J., Title, A.M., Schrijver, C.J., Tarbell, T.D., Tomczyk, S.: 2012, *Solar Phys.* **275**, 207. doi:10.1007/s11207-011-9834-2.

Schou, J., Scherrer, P.H., Bush, R.I., Wachter, R., Couvidat, S., Rabello-Soares, M.C., Bogart, R.S., Hoeksema, J.T., Liu, Y., Duvall, T.L. Jr., Akin, D.J., Allard, B.A., Miles, J.W., Rairden, R., Shine, R.A., Tarbell, T.D., Title, A.M., Wolfson, C.J., Elmore, D.F., Norton, A.A., Tomczyk, S.: 2012, *Solar Phys.* **275**, 229. doi:10.1007/s11207-011-9842-2.

Svalgaard, L., Duvall, T.L. Jr., Scherrer, P.H.: 1978, *Solar Phys.* **58**, 225. doi:10.1007/BF00157268.

Tran, T., Bertello, L., Ulrich, R.K., Evans, S.: 2005, *Astrophys. J. Suppl.* **156**, 295.

Ulrich, R.K.: 1992, In: Giampappa, M.S., Bookbinder, J.A. (eds.) *Proc. 7th Cambridge Workshop, Cool Stars, Stellar Systems, and the Sun*, **CS – 26**, Astron. Soc. Pacific, San Francisco, 265.

Ulrich, R.K., Bertello, L., Boyden, J.E., Webster, L.: 2009, *Solar Phys.* **255**, 53. doi:10.1007/s11207-008-9302-9.

Wang, Y.-M., Sheeley, N.R. Jr.: 1995, *Astrophys. J. Lett.* **447**, L143.